

Globally Stable Microresonator Turing Pattern Formation for Coherent High-Power THz Radiation On-Chip

Shu-Wei Huang,^{1,*} Jinghui Yang,^{1,†} Shang-Hua Yang,² Mingbin Yu,³ Dim-Lee Kwong,³ T. Zelevinsky,⁴ Mona Jarrahi,² and Chee Wei Wong^{1,‡}

¹*Fang Lu Mesoscopic Optics and Quantum Electronics Laboratory, University of California, Los Angeles, California 90095, USA*

²*Terahertz Electronics Laboratory, University of California, Los Angeles, California 90095, USA*

³*Institute of Microelectronics, A*STAR, Singapore 117865, Singapore*

⁴*Department of Physics, Columbia University, New York, New York 10027, USA*

(Received 9 August 2016; revised manuscript received 24 May 2017; published 5 October 2017)

In nonlinear microresonators driven by continuous-wave (cw) lasers, Turing patterns have been studied in the formalism of the Lugiato-Lefever equation with emphasis on their high coherence and exceptional robustness against perturbations. Destabilization of Turing patterns and the transition to spatiotemporal chaos, however, limit the available energy carried in the Turing rolls and prevent further harvest of their high coherence and robustness to noise. Here, we report a novel scheme to circumvent such destabilization, by incorporating the effect of local mode hybridizations, and we attain globally stable Turing pattern formation in chip-scale nonlinear oscillators with significantly enlarged parameter space, achieving a record-high power-conversion efficiency of 45% and an elevated peak-to-valley contrast of 100. The stationary Turing pattern is discretely tunable across 430 GHz on a THz carrier, with a fractional frequency sideband nonuniformity measured at 7.3×10^{-14} . We demonstrate the simultaneous microwave and optical coherence of the Turing rolls at different evolution stages through ultrafast optical correlation techniques. The free-running Turing-roll coherence, 9 kHz in 200 ms and 160 kHz in 20 minutes, is transferred onto a plasmonic photomixer for one of the highest-power THz coherent generations at room temperature, with 1.1% optical-to-THz power conversion. Its long-term stability can be further improved by more than 2 orders of magnitude, reaching an Allan deviation of 6×10^{-10} at 100 s, with a simple computer-aided slow feedback control. The demonstrated on-chip coherent high-power Turing-THz system is promising to find applications in astrophysics, medical imaging, and wireless communications.

DOI: [10.1103/PhysRevX.7.041002](https://doi.org/10.1103/PhysRevX.7.041002)

Subject Areas: Nanophysics, Nonlinear Dynamics, Optics

The spontaneous formation of stationary periodic patterns from homogeneous backgrounds first elucidated by Turing has served as the basis for developmental biology morphogenesis, chemical kinetics far from equilibrium, and the formation of fractals and chaos in nonlinear dynamics [1–3]. Of both conceptual importance and practical interest, optical Turing pattern formation has been theoretically proposed and investigated in continuous-wave (cw)-laser-pumped Kerr-active microresonators [4–7], with emphasis on its high coherence and exceptional robustness against perturbations. Generally, the Kerr-active microresonator is designed to possess anomalous group velocity dispersion (GVD) for convenient phase-matching fulfillment, and the

formation dynamics of the spontaneous patterns can be described by the Lugiato-Lefever equation [4]. As the driving laser is frequency tuned into the cavity resonance from the blue side, stable Turing rolls first spontaneously emerge from the background, then quickly destabilize into spatiotemporal chaos [8,9], and eventually transition into dissipative Kerr solitons [10–14] or Kerr frequency combs [15–18] (Fig. S1 in Ref. [19]). We note that the Turing roll in this dispersion regime, despite its optimally coherent properties [20], only exists in a limited phase space, and its quick destabilization into chaos limits the attainable power-conversion efficiency [Figs. 1(a) and 1(b)], preventing further harvest of the high coherence and the noise robustness of the Turing pattern.

To expand the stability zone and attain higher power conversion, we approach the spontaneous Turing pattern formation in a distinctly different way. Our Kerr-active microresonator is designed to possess a large globally normal GVD of $100 \text{ fs}^2/\text{mm}$ (Fig. S2 in Ref. [19]); thus, phase matching is strictly forbidden unless local dispersion anomalies are introduced to the system, providing additional GVD to balance the nonlinearity locally. In our high

*swhuang@seas.ucla.edu

†yangjh@seas.ucla.edu

‡cheewei.wong@ucla.edu

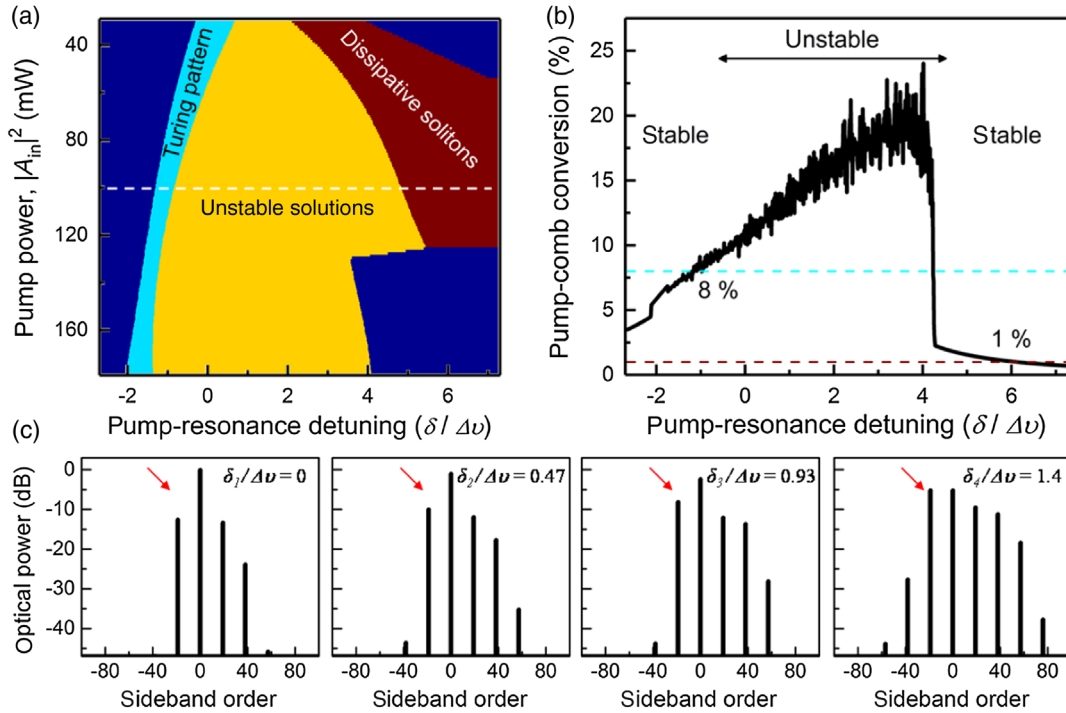


FIG. 1. (a) Stability diagram of the Turing pattern in the anomalous GVD regime. Light blue shows the region of the stable Turing pattern, yellow shows the region of breathers and spatiotemporal chaos, and red shows the region of the soliton and soliton molecules. (b) Pump-to-comb power-conversion efficiency along the white dashed line in (a), showing only 8% maximum power conversions to the Turing pattern before destabilization and transition to chaos happens. (c) Simulation of the Turing roll in the normal dispersion microresonator (1300 fs^2), where the Turing roll is excited by local mode hybridization. The red arrow points to the mode where local dispersion disruption is introduced in the Lugiato-Lefever model. It shows an apparent asymmetry and can be tuned further into resonance without triggering the subcomb growth and the associated Turing pattern destabilization, expanding the stability zone and opening the route to harness Turing pattern's high coherence and exceptional robustness at high optical powers. Note that the pump-resonance detuning used in the simulation is referenced to the cold cavity resonance frequency.

Q microresonator (loaded quality factor of 3.7×10^5), such anomalies result from the hybridization of two transverse modes (TM_{11} and TM_{21}) with distinct free spectral ranges (FSRs) when their resonant frequencies are in the vicinity of each other [21–27]. The spectral position of the mode hybridization defines the Turing pattern formation dynamics, and it can be changed by the design of the FSR difference. As the balance between the GVD and the Kerr nonlinearity is only fulfilled locally in the confined spectral range where mode hybridization occurs, subcomb growth and subsequent destabilization of the Turing pattern is avoided [Fig. 1(c)]. By enabling the deeper driving into resonance without transition into chaos or soliton states, the conversion efficiency from pump to Turing pattern can thus be significantly enhanced in our system. The mode-hybridization-mediated phase matching—by adjusting the relative frequency between the pump mode and the mode hybridization position—further enables the repetition rate of the Turing roll to be discretely tunable. Moreover, the Turing-roll spectra can exhibit controllable asymmetry through registering the pump mode on different sides of the first local-mode hybridization region ε_1 [Fig. 2(a)].

Here, we demonstrate, for the first time, the scheme of incorporating the mode hybridization effect to attain globally stable microresonator Turing patterns in chip-scale nonlinear nitride cavities with significantly enlarged parameter space, achieving an unprecedented pump depletion and a record-high power-conversion efficiency of 45% with an elevated peak-to-valley contrast of 100. We interrogate the commensurate and coherent nature of the spontaneous dissipative structure with ultrafast optical intensity autocorrelation, microwave spectral noise analysis, and heterodyne beating against a benchmark fiber frequency comb. The fractional-frequency-sideband non-uniformity of the Turing pattern is measured at 7.3×10^{-14} , with a short-term (200 ms sweep time) linewidth of 9 kHz and a long-term (over 20 minutes) fluctuation of 160 kHz in the free-running mode. The long-term stability can be further improved by more than 2 orders of magnitude, reaching an Allan deviation of 6×10^{-10} at 100 s, with a simple computer-aided slow feedback control. Towards THz applications, we then transfer the Turing pattern optical coherence to the THz carrier through a plasmonic ErAs:InGaAs photomixer, generating up to $600 \mu\text{W}$ THz radiation power at room temperature. The carrier frequency is discretely tunable over

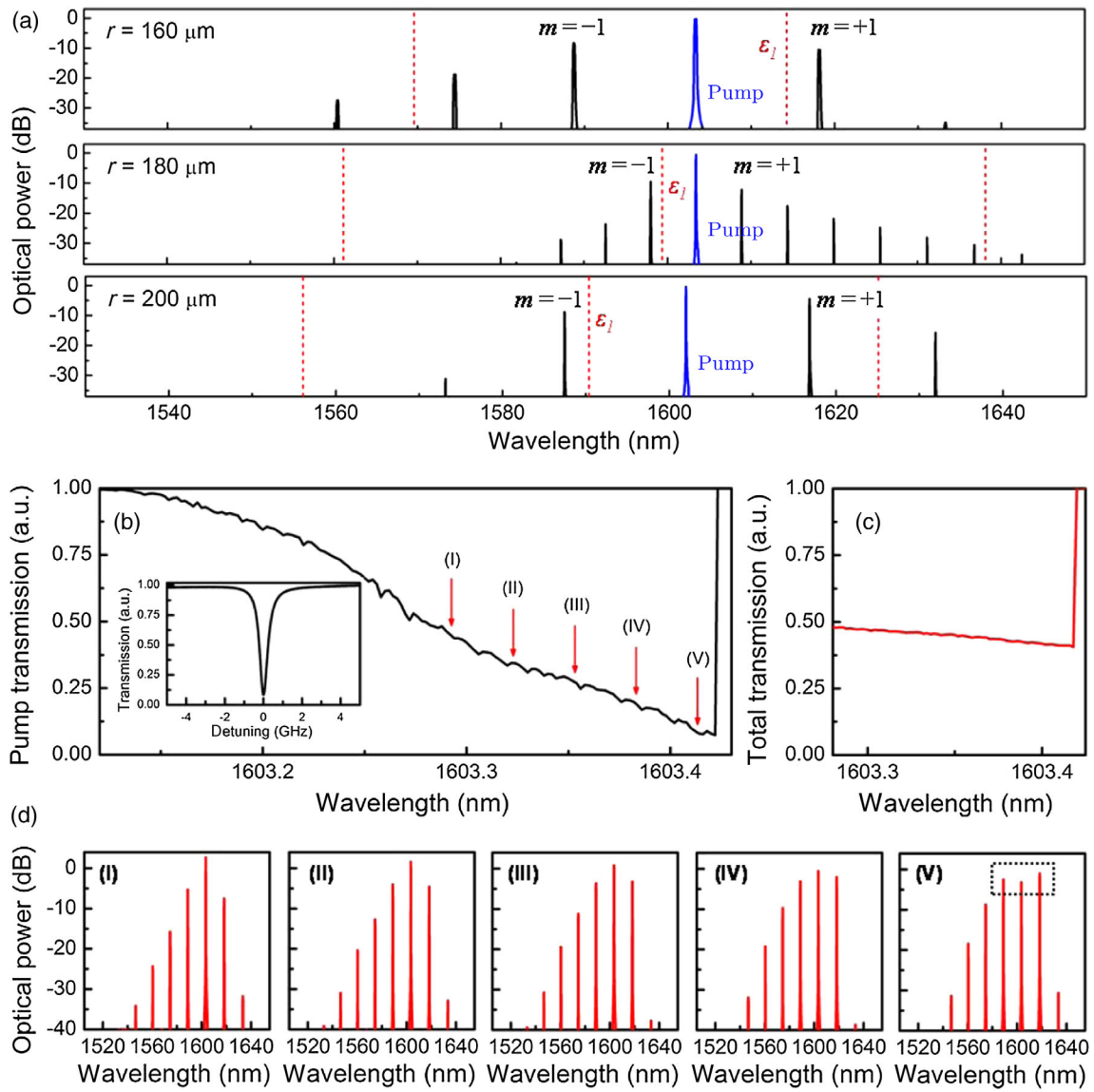


FIG. 2. (a) Turing rolls generated from ring resonators with different radii. Even though the GVD of the ring resonators differ by less than $2 \text{ fs}^2/\text{mm}$, the TM_{11} - TM_{21} mode hybridization positions (red dashed lines) with respect to the pump (blue lines) shift because of the change in the ring radii, resulting in abrupt dispersion variations locally and very different spontaneous Turing patterns. The Turing-roll repetition rates are 1.72 THz ($12 \times \text{FSR}$) for the $160 \mu\text{m}$ radius ring, 0.64 THz ($5 \times \text{FSR}$) for the $180 \mu\text{m}$ radius ring, and 1.72 THz ($15 \times \text{FSR}$) for the $200 \mu\text{m}$ radius ring. (b) Pump-cavity transmission as a function of the pump wavelength, labeling the detunings where different Turing-roll stages are generated. Inset: The cold resonance of the pump mode, measuring a loaded Lorentzian linewidth of 500 MHz and a loaded quality factor of 3.7×10^5 . (c) Total cavity transmission as a function of the pump wavelength in the range where the Turing roll is generated. Compared to the pump-cavity transmission, the total cavity transmission shows a less apparent decrease as the pump is tuned into the resonance, confirming an efficient power conversion from the pump to the generated Turing lines. (d) Example Turing-roll spectra at different stages. At stage V, even a highly depleted pump close to the resonance is observed in the measurement, illustrated in the dashed box.

a broadband from 1.14 THz to 1.57 THz . The demonstrated coherent high-power Turing-THz system offers the potential to be the room-temperature on-chip THz local oscillator for astrophysics, medical imaging, and wireless communication [28–33].

Here, a TM-polarized cw laser with an optical power of 29.5 dBm is frequency tuned from the blue side of the cavity resonance to trigger the Turing pattern formation. The

measured spectra of the spontaneous Turing patterns generated from ring resonators with different radii are shown in Fig. 2(a), with the pump illustrated in blue and the mode hybridization positions labeled as red dashed lines. Despite very similar GVD (β_2) from different radii ring resonators, the Turing patterns show spectral shapes that are distinct from each other. Specifically, the spectral lines on the side of the first mode hybridization position are suppressed because

of the increasing phase mismatch associated with the mode-hybridization-induced local dispersion disruption. With the first sideband pair ($m = \pm 1$) phase matched because of the additional contribution from the mode hybridization on mode 1, the phase-matching condition can be written as

$$\Delta k(2\omega_0 - \omega_1 - \omega_{-1}) = \beta_2 \Delta^2 + \gamma P_{\text{int}} - \varepsilon = 0,$$

where ε represents the contribution from the mode hybridization, Δ the Turing-roll repetition rate, γ the nonlinear Kerr coefficient, and P_{int} the intracavity power. Here, $k_1 = k_0 + \beta' \Delta + (\beta_2/2)\Delta^2 + \varepsilon$ and $k_m = k_0 + \beta'(m\Delta) + (\beta_2/2)(m\Delta)^2$, where β' is the group velocity. Then, the phase-matching condition for the first cascaded four-wave mixing on *either* side of the pump can be written as

$$\Delta k(2\omega_1 - \omega_2 - \omega_0) = \beta_2 \Delta^2 + \gamma P_{\text{int}} + 2\varepsilon = 3\varepsilon,$$

$$\Delta k(2\omega_{-1} - \omega_0 - \omega_{-2}) = \beta_2 \Delta^2 + \gamma P_{\text{int}} = \varepsilon.$$

The phase mismatch on the side of the mode-crossing position is 3 times larger than the other process; thus, the symmetry of the Turing-roll spectra is broken. Similar symmetry breaking by mode hybridization has also been demonstrated in microwave photonics recently [34]. Turing-roll repetition rates also show dramatic variations (≈ 640 GHz in the 180 μm radius ring and ≈ 1.72 THz in the 160 μm and 200 μm rings) that cannot be solely explained by the change in the cavity round-trip time. These features are direct consequences of the unique phase-matching configuration employed in our design, with critical roles in the efficient coherence transfer from Turing pattern to THz radiation to be detailed later. Note that the mode-hybridization-induced local dispersion disruption ε can be dynamically tuned by changing the temperature of the microresonator, thereby providing an additional dimension to control the Turing pattern formation dynamics (detailed in Ref. [19]).

Next, we focus on the results generated from the 160 μm radius ring because of its energy concentration in the wavelength range shorter than 1570 nm, overlapping better with the spectral response of our plasmonic photomixer discussed later. Figures 2(b) and 2(c) show the pump and total transmitted intensities, measured simultaneously for different detunings. The pump transmission shows a triangular tuning curve with a strong dip from normalized unity into $\approx 10\%$ of the original transmission, while the total transmission shows only a small drop from 48% to 41%—this provides evidence of the efficient total energy transfer from the pump into the complete Turing pattern sidebands. To examine this further, Fig. 2(d) plots the corresponding Turing-roll spectra at different detuning stages: Stable spontaneous Turing patterns are observed without any sign of destabilization at all detunings. The power-conversion efficiency, defined as the integrated power of the output Turing roll divided by the on-chip pump power, reaches as

high as 45% at stage III (detailed in Ref. [19]). Closer to resonance at stage V, an even stronger pump depletion is achieved, with the pump intensity 2 dB lower than even the first modulation sidebands.

We conduct a series of ultrafast optical intensity auto-correlation (IAC) measurements, as shown in Fig. 3(a), to investigate the temporal structure of the Turing patterns at different evolving stages. At all the stages, stable and strong quasisinusoidal oscillations are observed. While pumping closer to resonance results in a monotonic increase in the pump depletion [Fig. 2(d)], counterintuitively, the IAC traces show a discernible minimum background between stage II and stage III. As elaborated on later, it is a direct consequence of strong pump depletion. At stage III, a peak-to-valley intensity contrast ratio of more than 100 is achieved (Fig. S8 in Ref. [19]). We next perform extensive measurements to examine the coherence of the spontaneous Turing formation, illustrated in Figs. 3(b)–3(e). The RF-amplitude noise spectra of the Turing pattern up to 3 GHz, 6 times the cavity linewidth, shows an absence of RF peaks and a noise level at the instrumentation detection background limit, indicative of the existence of a single Turing-roll family with commensurate repetition rates [Fig. 3(b)]. We further heterodyne beat the Turing sidebands ($m = \pm 1$ and pump) against a benchmark fiber frequency comb (see Appendix C) and perform ratio counting of the sidebands to interrogate the frequency uniformity, which sets the fundamental limit on the coherence transfer from the Turing pattern [Fig. 3(c)]. When the Turing-roll repetition rate is made nondivisible by the fiber frequency-comb spacing, the beat frequencies of consecutive sidebands will be an arithmetic sequence. Namely, $\delta_2 = \delta_1 + \Delta = \delta_0 + 2\Delta$. Here, we make the common difference Δ equal to 1 MHz. Ideally, the ratio between $\delta_2 - \delta_0$ and $\delta_1 - \delta_0$, R , should be 2, and deviation from this ratio, ε_R , is a measure of the sideband frequency nonuniformity, $\varepsilon = \varepsilon_R \cdot \Delta$. Excellent sideband uniformity of the Turing pattern is observed at all evolving stages, with the average nonuniformity measured at 125 mHz, or 7.3×10^{-14} when referenced to the Turing pattern repetition rate at 1.72 THz [Fig. 3(c)]. Figure 3(d) next shows the self-heterodyne beat note of the first sideband (see Appendix C), demonstrating the Turing lines down to a pump-coherence-limited linewidth of 500 kHz. The linewidth measurements independently confirm the good coherence of the Turing rolls at all detunings. Figure 3(e) also shows the real-time power monitoring of the four strongest sidebands. All sidebands present similar intensity noise of less than 1% (integrated from 100 Hz to 100 MHz), and no cyclic energy exchange between sidebands is observed, excluding the possibility of breathing dynamics with conserved total power and supporting the evidence of stationary Turing pattern formation with an extensive stability zone.

To examine whether the temporal shape of the spontaneous Turing pattern is subjected to the perturbation in the initial condition and the pump detuning scan, we performed

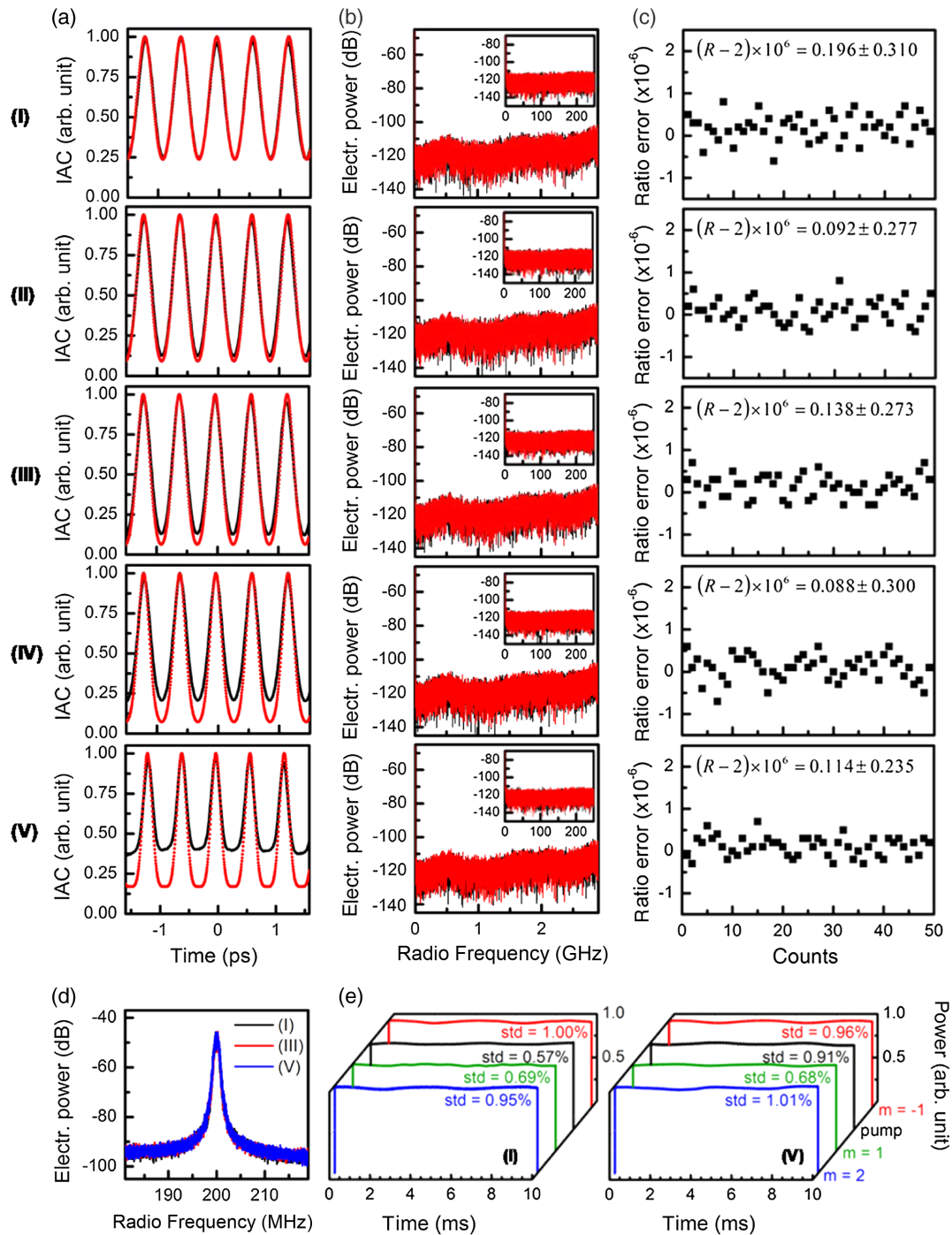


FIG. 3. (a) IAC traces of the Turing rolls at different stages. The red dashed lines are the ideal traces calculated from the spectra, while the black curves are the measured traces. As the sidebands grow, the deviations between the measured and calculated IAC traces also increase. (b) To examine the emergence of incommensurate subcombs, RF amplitude noise spectra of the Turing rolls (black curve) along with the detector background (red curve) are measured up to 3 GHz, 6 times the cavity linewidth. No apparent amplitude noise is observed, verifying the existence of the commensurate subcombs. Inset: Zoom-in RF amplitude noise spectra up to 250 MHz, at the instrumentation detection noise floor. (c) To probe the equidistance of the Turing rolls, the beat notes between the three Turing-roll sidebands (pump, $m = 1$, and $m = 2$) and the adjacent fiber-laser frequency-comb lines are measured, and the ratio errors are presented. The small deviation from the ideal ratio R of 2 [R defined in the main text as $(\delta_2 - \delta_0)/(\delta_1 - \delta_0)$] verifies the Turing pattern's excellent uniformity. The average nonuniformity is measured at 125 mHz, or 7.3×10^{-14} when referenced to the Turing pattern repetition rate at 1.72 THz. (d) The linewidth of the first sideband is measured at 500 kHz, limited by the coherence of the pump laser, by the self-heterodyne technique at different stages. No linewidth broadening is observed, independently confirming that the coherence of the Turing roll is maintained at all evolving stages. (e) Power fluctuation of individual sidebands at the stages I (left) and V (right) with a sampling rate of 250 MHz, ruling out the possibility of breathing solutions.

the IAC measurements at three different tuning speeds and two independent starts. Each of the Turing IAC dynamics remains identical (Fig. S9 in Ref. [19]), illustrating the good robustness of the Turing patterns. To understand the dynamics better, ideal IAC traces from transform-limited Turing patterns are superimposed onto the measured IAC traces [Fig. 3(a), in red]. As the Turing pattern is driven closer to resonance, there is increasing discrepancy of the measured pattern from the transform limit. The change of temporal shapes without the coherence loss implies that the spectral phase of the Turing pattern varies at the different evolving stages; thus, different external-phase-compensation strategies are necessary if the temporal properties of the Turing pattern are to be fully utilized. The spectral phase variation can be understood as the consequence of the pump phase slip around the resonance. The relationship between the output and the intracavity pump power can be written as

$$A_{p,\text{out}} = -\frac{\gamma_c - \gamma_\alpha - i\delta}{\sqrt{2}\gamma_c} \sqrt{T_R} A_{p,\text{cav}},$$

where γ_c and γ_α are the half-width half-maximum linewidths associated with the coupling losses and the intrinsic cavity losses, respectively. In our microresonator, $\gamma_c = 160$ MHz and $\gamma_\alpha = 90$ MHz. The output pump will experience a π phase shift as it traverses through the resonance (Fig. S9a in Ref. [19]). Such a phase slip is due to the interference between the intracavity and the input pump; thus, the other sidebands of the Turing roll will not experience such a phase shift. This additional pump phase slip results in the observed change of temporal structure. The distinct responses to dispersion at different Turing states (illustrated in Fig. S10 in Ref. [19]) are well captured by considering the pump phase offset (Fig. S11b in Ref. [19]). Note that most of the phase slip happens very close to cavity resonance; thus, the observation of its effect is attributed to the unique design of our microresonator, which utilizes the local mode hybridization to fulfill the phase matching of spontaneous Turing pattern formation and greatly suppresses the Turing pattern destabilization even when the pump is deep into the resonance.

The robustness, tunability, good coherence, and high efficiency of the demonstrated Turing roll make it an excellent photomixer pump for narrow-linewidth-tunable THz radiation. Different from deriving the pump from a mode-locked laser [32], our Turing pattern offers the advantage of efficient power use and reduced system complexity as its quasisinusoidal intensity profile (Fig. S8 in Ref. [19]) is directly applicable as a photomixer pump. Other photomixer pump sources [35] include independent lasers with frequency stabilization [36,37], single lasers with active high-speed phase modulation [31], and tunable dual-mode lasers [38–42]. While phase locking two independent lasers to external frequency references can potentially provide the ultimate coherence, it suffers from greatly increased system complexity. Using a single laser with active phase

modulation simplifies the system, but high-speed phase modulation with a bandwidth higher than 1 THz is technologically challenging. A tunable dual-mode laser is attractive in its compact footprint and broadband tunability; however, it has a large long-term frequency drift due to the uncommon paths taken by the two modes, and solving it again requires a sophisticated phase-locking technique. Our demonstrated Turing roll provides an alternative platform as it not only is intrinsically compatible with high power operation but also offers a balance between highest coherence and lowest system complexity.

To characterize the stability of the free-running Turing-roll repetition rate, which determines the linewidth and fluctuation of the THz radiation, we beat the pump and one of the sidebands with the adjacent fiber-laser frequency-comb lines and electrically mix the two signals to get the beat note at the frequency difference, as shown in Fig. S13 in Ref. [19]. Figure 4 shows the long-term frequency fluctuation, measuring a root-mean-square frequency fluctuation of 160 kHz over 20 minutes. The left inset shows the linewidth of the beat note with a sweep time of 200 ms, measuring a narrow FWHM linewidth of 9 kHz; the right inset shows the frequency stability of the beat note, measuring an Allan deviation of $1.15 \times 10^{-8} \cdot \sqrt{\tau}$ when referenced to the THz carrier. Its long-term stability can be further improved by a cost-effective computer-aided slow feedback control of the Turing sideband power. The feedback bandwidth is about 1 Hz. As the microresonator is housed in a temperature-controlled enclosure, we attribute the instability of the Turing-roll repetition rate mainly to the effects associated with the fluctuation of intracavity power, which, at the same time, has major impact on the Turing sideband power. Thus, by stabilizing the Turing sideband power, the fluctuation of intracavity power is reduced, and

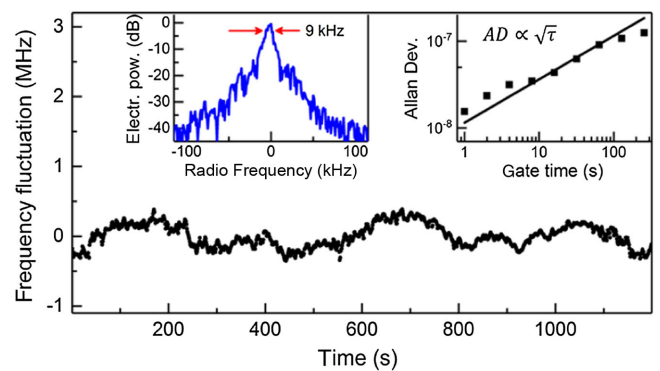


FIG. 4. Long-term frequency fluctuation of the first sideband with respect to the pump in the free-running mode, showing the repetition rate fluctuation of 160 kHz over 20 minutes. The left inset shows the linewidth of the beat note with a sweep time of 200 ms, measuring a narrow FWHM linewidth of 9 kHz; the right inset shows the frequency stability of the beat note, measuring an Allan deviation of $1.15 \times 10^{-8} \cdot \sqrt{\tau}$ when referenced to the THz carrier.

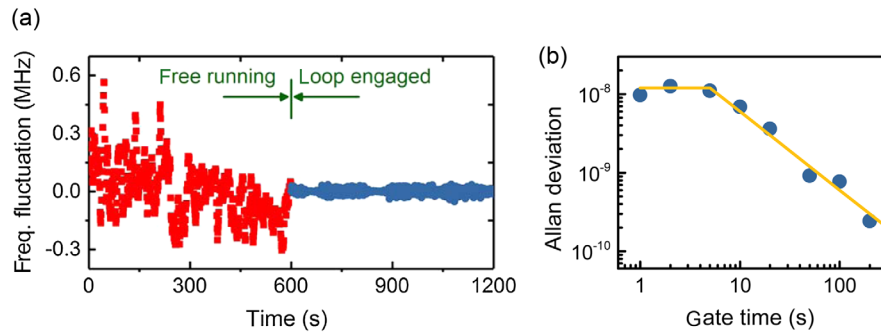


FIG. 5. (a) Long-term frequency fluctuation of the first sideband with respect to the pump engaging (blue) and without engaging (red) the computer-aided slow feedback control, counted with a gate time of 1 second. (b) Allan deviation of the stabilized THz frequency, measuring a plateau of 1.2×10^{-8} for gate times shorter than 5 seconds and a roll-off of $6 \times 10^{-8}/\tau$ for longer gate times.

consequently, the long-term stability of the Turing-roll repetition rate is improved (Fig. S16). When the feedback loop is engaged, the frequency stability is greatly improved, as shown in Fig. 5(a). Figure 5(b) shows the Allan deviation after stabilization, measuring an improvement of more than 2 orders of magnitude and reaching 6×10^{-10} at 100 s with an inverse linear dependence on the gate time.

To convert the Turing pattern into the THz radiation, we fabricate an ErAs:InGaAs plasmonic photomixer [Fig. 6(a)], which features a good spectral response from 0.8 to 1.6 THz due to the logarithmic spiral antenna design [43]. A C/L WDM filter, followed by an erbium-doped fiber amplifier (EDFA), is used to selectively amplify the

Turing pattern sidebands in the 1530–1565-nm C-band range. Note that the EDFA is necessary only because our current Si_3N_4 microresonator has a strong Q -factor roll-off in the C-band; thus, we are limited to pumping it in the L-band. Figure 6(b) shows four examples illustrating the tunability of the Turing-roll repetition rate (1.14–1.57 THz), which in turn determines the THz frequency, by tuning the chip temperature or the pump wavelength. Figure 6(c) plots the room-temperature radiated THz power as a function of the optical pump power, showing a nearly quadratic dependence even at the maximum available pump power of 54 mW, without much saturation roll-off in the THz generation. Up to $600 \mu\text{W}$ THz

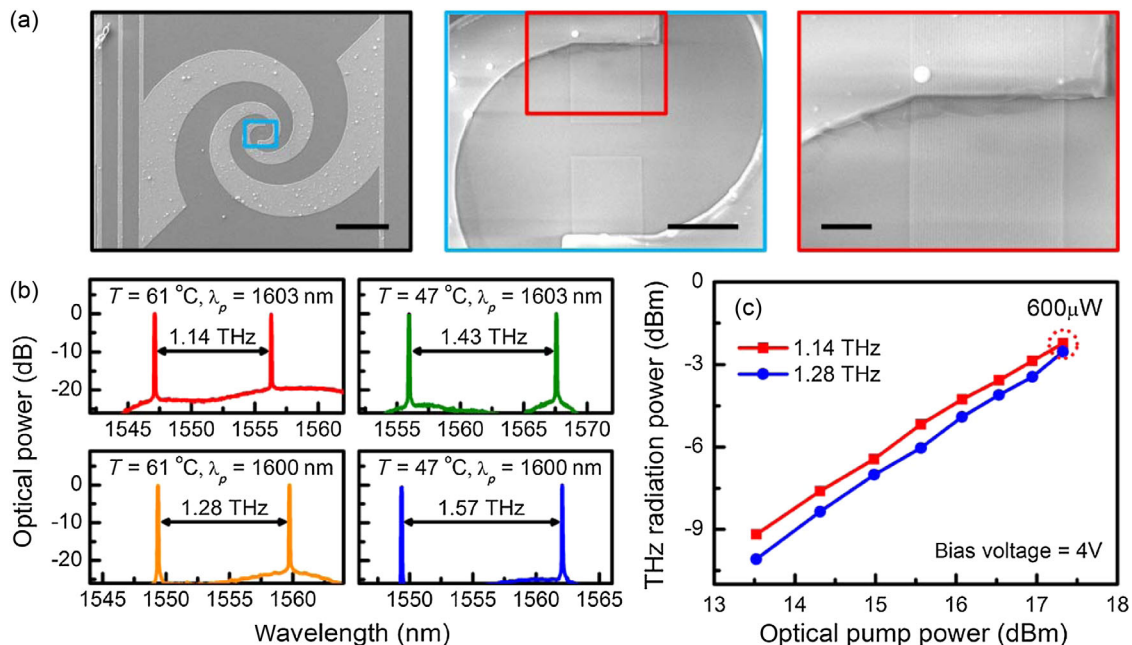


FIG. 6. (a) Scanning electron micrographs of the fabricated plasmonic photomixer with a logarithmic spiral antenna integrated with plasmonic contact electrodes on an ErAs:InGaAs substrate. Scale bars from left to right: $100 \mu\text{m}$, $10 \mu\text{m}$, and $3 \mu\text{m}$. (b) Turing-roll repetition rate, and hence the generated THz frequency, can be tuned by changing the pump wavelength and the resonator temperature. (c) THz radiation power as a function of optical pump power. Power-conversion efficiency of 1.1% can be obtained with an optical pump power of 54 mW.

radiation is generated with an optical-to-THz power-conversion efficiency of 1.1%.

In summary, we demonstrate the scheme of incorporating the mode hybridization effect to attain globally stable microresonator Turing patterns in chip-scale nonlinear nitride cavities with significantly enlarged parameter spaces, achieving an unprecedented pump depletion and a record-high power-conversion efficiency of 45% with an elevated peak-to-valley contrast of 100. Controllable asymmetry in the Turing-roll spectrum is also demonstrated. The fractional frequency sideband nonuniformity of the Turing pattern is measured down to 7.3×10^{-14} , with a short-term (200 ms sweep time) linewidth of 9 kHz and a long-term (over 20 minutes) fluctuation of 160 kHz in the free-running mode. The long-term stability can be further improved to sub-kHz with a simple computer-aided slow feedback control. We observe that the temporal shapes of the Turing patterns change with respect to pump detuning, not because of the coherence loss but because of the pump phase slip near the cavity resonance. The robustness, tunability, good coherence, and high efficiency of the demonstrated Turing pattern make it an excellent photomixer pump for narrow-linewidth-tunable THz radiation. Pumping a novel ErAs:InGaAs plasmonic photomixer, we then transfer the Turing pattern optical coherence to the THz carrier and generate up to 600 μ W THz radiation power at room temperature. The carrier frequency is discretely tunable over a broadband from 1.14 THz to 1.57 THz. The demonstrated coherent high-power Turing-THz system has the potential to be the room-temperature on-chip THz local oscillator for astrophysics, medical imaging, and wireless communication.

ACKNOWLEDGMENTS

The authors thank Bart H. McGuyer for discussions. The authors acknowledge funding support from Office of Naval Research (ONR) Grant No. N00014-14-1-0041, Air Force Office of Scientific Research (AFOSR) Young Investigator Grant No. FA9550-15-1-0081, Defense Advanced Research Projects Agency (DARPA) Grant No. HR0011-15-2-0014, and National Science Foundation (NSF) Grant No. PHY-1349725.

S.-W. H. and J. Y. contributed equally to this work.

APPENDIX A: Si_3N_4 MICRORESONATOR FABRICATION

First, a 3 μ m-thick oxide layer is deposited via plasma-enhanced chemical vapor deposition (PECVD) on *p*-type 8" silicon wafers to serve as the under-cladding oxide. Then, low-pressure chemical vapor deposition (LPCVD) is used to deposit a 725-nm silicon nitride for the ring resonators, with a gas mixture of SiH_2Cl_2 and NH_3 . The resulting silicon nitride layer is patterned by optimized 248-nm deep-ultraviolet lithography and etched down to the

buried oxide layer via optimized reactive-ion dry etching. Under a scanning electron microscope, the etched sidewall verticality is measured to be 88° , and the residual sidewall imperfections result in the mode hybridization effect described in the main text. Next, the silicon nitride ring resonators are over-cladded with a 3 μ m-thick oxide layer, deposited initially with LPCVD (500 nm) and then with PECVD (2500 nm). The propagation loss of the silicon nitride waveguide is measured to be 0.2 dB/cm at the pump wavelength. Cold cavity properties of the microresonator are precisely characterized by a hydrogen-cyanide-referenced swept-wavelength interferometer (Ref. [19]).

APPENDIX B: ULTRAFAST INTENSITY AUTOCORRELATION AND SELF-HETERODYNE CHARACTERIZATION

The optical intensity autocorrelator consists of a 1-mm-thick β -BBO crystal, supporting a bandwidth of 200 nm, and a silicon avalanche photodiode, supporting a sensitivity of 100 μ W. The setup is configured in a noncollinear geometry, and careful checks are done before measurements to ensure only background-free second-harmonic signals are collected. The use of dispersive optics is also minimized such that the additional dispersion introduced to the pulse is only -50 fs². To further confirm the coherence of the Turing sidebands, self-heterodyne linewidth measurements are performed with detailed setup, as shown in Ref. [19]. With a 200-MHz acousto-optic modulator and 24.5 μ s delay provided by a 5-km single-mode optical fiber, our self-heterodyne setup shows a minimum linewidth at 13 kHz, about 40 times smaller than the pump laser linewidth (≈ 500 kHz).

APPENDIX C: TURING PATTERN UNIFORMITY MEASUREMENTS AGAINST A FIBER FREQUENCY COMB

Sideband frequency uniformity of the Turing pattern is measured by heterodyne referencing against a benchmark optical-fiber-laser frequency comb, Menlo FC1500-250-WG. As detailed in Ref. [19], the spontaneous Turing roll is split into three beat-detection units ($m = \pm 1$ and pump) with more than 40-dB signal-to-noise ratio at 100-kHz resolution bandwidth. The sideband beat notes (δ_1 and δ_2) are mixed with the pump beat note (δ_0) to cancel the residual pump frequency instability, with the frequency counter operating in the ratio-counting mode to circumvent synchronization of the simultaneous beat-note measurements.

APPENDIX D: PLASMONIC PHOTOMIXER FABRICATION

The plasmonic contact electrode gratings are designed to have 200-nm pitch, 100-nm metal width, 5/45 nm Ti/Au height, and 250-nm-thick silicon nitride antireflection (AR) coating. They are patterned with electron-beam lithography

followed by deposition of Ti/Au and liftoff. A 250-nm silicon nitride AR coating is then deposited with PECVD. Contact vias are patterned with optical lithography and etched via dry plasma etching. Finally, the logarithmic spiral antennas and bias lines are patterned again with optical lithography, followed by deposition of Ti/Au and liftoff. The fabricated plasmonic photomixers are then mounted on a hyper-hemispherical silicon lens to improve the THz radiation collection.

-
- [1] A. M. Turing, *The Chemical Basis of Morphogenesis*, *Phil. Trans. R. Soc. B* **237**, 37 (1952).
- [2] S. Kondo and T. Miura, *Reaction-Diffusion Model as a Framework for Understanding Biological Pattern Formation*, *Science* **329**, 1616 (2010).
- [3] A. W. Liehr, *Dissipative Solitons in Reaction Diffusion Systems* (Springer, Berlin, Heidelberg, 2013).
- [4] L. A. Lugiato and R. Lefever, *Spatial Dissipative Structures in Passive Optical Systems*, *Phys. Rev. Lett.* **58**, 2209 (1987).
- [5] A. J. Scroggie, W. J. Firth, G. S. McDonald, M. Tlidi, R. Lefever, and L. A. Lugiato, *Pattern Formation in a Passive Kerr Cavity*, *Chaos Solitons Fractals* **4**, 1323 (1994).
- [6] C. Godey, I. V. Balakireva, A. Coillet, and Y. K. Chembo, *Stability Analysis of the Spatiotemporal Lugiato-Lefever Model for Kerr Optical Frequency Combs in the Anomalous and Normal Dispersion Regimes*, *Phys. Rev. A* **89**, 063814 (2014).
- [7] A. Coillet, I. Balakireva, R. Henriët, K. Saleh, L. Larger, J. M. Dudley, C. R. Menyuk, and Y. K. Chembo, *Azimuthal Turing Patterns, Bright and Dark Cavity Solitons in Kerr Combs Generated with Whispering-Gallery-Mode Resonators*, *IEEE Photonics J.* **5**, 6100409 (2013).
- [8] A. B. Matsko, W. Liang, A. A. Savchenkov, and L. Maleki, *Chaotic Dynamics of Frequency Combs Generated with Continuously Pumped Nonlinear Microresonators*, *Opt. Lett.* **38**, 525 (2013).
- [9] A. Coillet and Y. K. Chembo, *Routes to Spatiotemporal Chaos in Kerr Optical Frequency Combs*, *Chaos* **24**, 013113 (2014).
- [10] T. Herr, V. Brasch, J. D. Jost, C. Y. Wang, N. M. Kondratiev, M. L. Gorodetsky, and T. J. Kippenberg, *Temporal Solitons in Optical Microresonators*, *Nat. Photonics* **8**, 145 (2014).
- [11] S.-W. Huang, H. Zhou, J. Yang, J. F. McMillan, A. Matsko, M. Yu, D.-L. Kwong, L. Maleki, and C. W. Wong, *Mode-Locked Ultrashort Pulse Generation from On-Chip Normal Dispersion Microresonators*, *Phys. Rev. Lett.* **114**, 053901 (2015).
- [12] X. Xue, Y. Xuan, Y. Liu, P.-H. Wang, S. Chen, J. Wang, D. E. Leaird, M. Qi, and A. M. Weiner, *Mode-Locked Dark Pulse Kerr Combs in Normal-Dispersion Microresonators*, *Nat. Photonics* **9**, 594 (2015).
- [13] X. Yi, Q.-F. Yang, K. Y. Yang, M.-G. Suh, and K. Vahala, *Soliton Frequency Comb at Microwave Rates in a High-Q Silica Microresonator*, *Optica* **2**, 1078 (2015).
- [14] C. Joshi, J. K. Jang, K. Luke, X. Ji, S. A. Miller, A. Klenner, Y. Okawachi, M. Lipson, and A. L. Gaeta, *Thermally Controlled Comb Generation and Soliton Modelocking in Microresonators*, *Opt. Lett.* **41**, 2565 (2016).
- [15] T. J. Kippenberg, R. Holzwarth, and S. A. Diddams, *Microresonator-Based Optical Frequency Combs*, *Science* **332**, 555 (2011).
- [16] S.-W. Huang, J. Yang, M. Yu, B. H. McGuyer, D.-L. Kwong, T. Zelevinsky, and C. W. Wong, *A Broadband Chip-Scale Optical Frequency Synthesizer at 2.7×10^{-16} Relative Uncertainty*, *Sci. Adv.* **2**, e1501489 (2016).
- [17] P. Del'Haye, A. Coillet, T. Fortier, K. Beha, D. C. Cole, K. Y. Yang, H. Lee, K. J. Vahala, S. B. Papp, and S. A. Diddams, *Phase-Coherent Microwave-to-Optical Link with a Self-Referenced Microcomb*, *Nat. Photonics* **10**, 516 (2016).
- [18] J. Lim, S.-W. Huang, A. K. Vinod, P. Mortazavian, M. Yu, D.-L. Kwong, A. A. Savchenkov, A. B. Matsko, L. Maleki, and C. W. Wong, *A Stabilized Chip-Scale Kerr Frequency Comb via a High-Q Reference Photonic Microresonator*, *Opt. Lett.* **41**, 3706 (2016).
- [19] See Supplemental Material at <http://link.aps.org/supplemental/10.1103/PhysRevX.7.041002> for measurement details and numerical analyses.
- [20] J. Pfeifle, A. Coillet, R. Henriët, K. Saleh, P. Schindler, C. Weimann, W. Freude, I. V. Balakireva, L. Larger, C. Koos, and Y. K. Chembo, *Optimally Coherent Kerr Combs Generated with Crystalline Whispering Gallery Mode Resonators for Ultrahigh Capacity Fiber Communications*, *Phys. Rev. Lett.* **114**, 093902 (2015).
- [21] A. A. Savchenkov, A. B. Matsko, W. Liang, V. S. Ilchenko, D. Seidel, and L. Maleki, *Kerr Frequency Comb Generation in Overmoded Resonators*, *Opt. Express* **20**, 27290 (2012).
- [22] I. S. Grudinín, L. Baumgartel, and N. Yu, *Impact of Cavity Spectrum on Span in Microresonator Frequency Combs*, *Opt. Express* **21**, 26929 (2013).
- [23] Y. Liu, Y. Xuan, X. Xue, P.-H. Wang, S. Chen, A. J. Metcalf, J. Wang, D. E. Leaird, M. Qi, and A. M. Weiner, *Investigation of Mode Coupling in Normal-Dispersion Silicon Nitride Microresonators for Kerr Frequency Comb Generation*, *Optica* **1**, 137 (2014).
- [24] S. A. Miller, Y. Okawachi, S. Ramelow, K. Luke, A. Dutt, A. Farsi, A. L. Gaeta, and M. Lipson, *Tunable Frequency Combs Based on Dual Microring Resonators*, *Opt. Express* **23**, 21527 (2015).
- [25] X. Xue, Y. Xuan, P.-H. Wang, Y. Liu, D. E. Leaird, M. Qi, and A. M. Weiner, *Normal-Dispersion Microcombs Enabled by Controllable Mode Interactions*, *Laser Photonics Rev.* **9**, L23 (2015).
- [26] S.-W. Huang, J. Yang, J. Lim, H. Zhou, M. Yu, D.-L. Kwong, and C. W. Wong, *A Low-Phase-Noise 18 GHz Kerr Frequency Microcomb Phase-Locked over 65 THz*, *Sci. Rep.* **5**, 13355 (2015).
- [27] S.-W. Huang, H. Liu, J. Yang, M. Yu, D.-L. Kwong, and C. W. Wong, *Smooth Coherent Kerr Frequency Combs Generation with Broadly Tunable Pump by Higher Order Mode Suppression*, *Sci. Rep.* **6**, 26255 (2016).
- [28] K. Unterrainer, A. Benz, J. Darmo, C. Deutsch, G. Fasching, J. Kroll, D. P. Kelly, M. Martl, T. Müller, W. Parz *et al.*, *Terahertz Quantum Cascade Devices: From Intersubband Transition to Microcavity Laser*, *IEEE J. Sel. Top. Quantum Electron.* **14**, 307 (2008).

- [29] S. Jung, A. Jiang, Y. Jiang, K. Vijayraghavan, X. Wang, M. Troccoli, and M. A. Belkin, *Broadly Tunable Monolithic Room-Temperature Terahertz Quantum Cascade Laser Sources*, *Nat. Commun.* **5**, 4267 (2014).
- [30] C. Sirtori, S. Barbieri, and R. Colombelli, *Wave Engineering with THz Quantum Cascade Lasers*, *Nat. Photonics* **7**, 691 (2013).
- [31] J. Darmo, V. Tamosiunas, G. Fasching, J. Kröll, K. Unterrainer, M. Beck, M. Giovannini, J. Faist, C. Kremser, and P. Debbage, *Imaging with a Terahertz Quantum Cascade Laser*, *Opt. Express* **12**, 1879 (2004).
- [32] S. Koenig, D. Lopez-Diaz, J. Antes, F. Boes, R. Henneberger, A. Leuther, A. Tessmann, R. Schmogrow, D. Hillerkuss, R. Palmer *et al.*, *Wireless Sub-THz Communication System with High Data Rate*, *Nat. Photonics* **7**, 977 (2013).
- [33] Y. Yoshimizu, S. Hisatake, S. Kuwano, J. Terada, N. Yoshimoto, and T. Nagatsuma, *Wireless Transmission Using Coherent Terahertz Wave with Phase Stabilization*, *IEICE Electron. Express* **10**, 578 (2013).
- [34] A. Rueda, F. Sedlmeir, M. C. Collodo, U. Vogl, B. Stiller, G. Schunk, D. V. Strelakov, C. Marquardt, J. M. Fink, O. Painter, G. Leuchs, and H. G. L. Schwefel, *Efficient Microwave to Optical Photon Conversion: An Electro-Optical Realization*, *Optica* **3**, 597 (2016).
- [35] T. Nagatsuma, G. Ducournau, and C. C. Renaud, *Advances in Terahertz Communications Accelerated by Photonics*, *Nat. Photonics* **10**, 371 (2016).
- [36] Q. Quraishi, M. Griebel, T. Kleine-Ostmann, and R. Bratschitsch, *Generation of Phase-Locked and Tunable Continuous-Wave Radiation in the Terahertz Regime*, *Opt. Lett.* **30**, 3231 (2005).
- [37] J.-F. Cliche, B. Shillue, M. Tetu, and M. Poulin, *A 100-GHz-Tunable Photonic Millimeter Wave Synthesizer for the Atacama Large Millimeter Array Radio Telescope*, in Proceedings of IEEE/MTT-S International Microwave Symposium, Honolulu, 2007 (IEEE, New York, 2007), p. 349.
- [38] H.-J. Song, N. Shimizu, and T. Nagatsuma, *Generation of Two-Mode Optical Signals with Broadband Frequency Tunability and Low Spurious Signal Level*, *Opt. Express* **15**, 14901 (2007).
- [39] A. Rolland, G. Loas, M. Brunel, L. Frein, M. Vallet, and M. Alouini, *Non-linear Optoelectronic Phase-Locked Loop for Stabilization of Opto-Millimeter Waves: Towards a Narrow Linewidth Tunable THz Source*, *Opt. Express* **19**, 17944 (2011).
- [40] G. Pillet, L. Morvan, M. Brunel, F. Bretenaker, D. Dolfi, M. Vallet, J. P. Huignard, and A. L. Floch, *Dual-Frequency Laser at 1.5 μm for Optical Distribution and Generation of High-Purity Microwave Signals*, *J. Lightwave Technol.* **26**, 2764 (2008).
- [41] G. Danion, C. Hamel, L. Frein, F. Bondu, G. Loas, and M. Alouini, *Dual Frequency Laser with Two Continuously and Widely Tunable Frequencies for Optical Referencing of GHz to THz Beatnotes*, *Opt. Express* **22**, 17673 (2014).
- [42] H. Shao, S. Keyvaninia, M. Vanwolleghem, G. Ducournau, X. Jiang, G. Morthier, J.-F. Lampin, and G. Roelkens, *Heterogeneously Integrated III-V/Silicon Dual-Mode Distributed Feedback Laser Array for Terahertz Generation*, *Opt. Lett.* **39**, 6403 (2014).
- [43] C. W. Berry, M. R. Hashemi, S. Preu, H. Lu, A. C. Gossard, and M. Jarrahi, *High Power Terahertz Generation Using 1550 nm Plasmonic Photomixers*, *Appl. Phys. Lett.* **105**, 011121 (2014).

Supplemental Material for

Globally stable microresonator Turing pattern formation for coherent high-power THz radiation on-chip

Shu-Wei Huang^{1,*,+}, Jinghui Yang^{1,*,+}, Shang-Hua Yang², Mingbin Yu³, Dim-Lee Kwong³, T. Zelevinsky⁴, Mona Jarrahi², and Chee Wei Wong^{1,*}

¹ Fang Lu Mesoscopic Optics and Quantum Electronics Laboratory, University of California, Los Angeles, CA 90095, USA.

² Terahertz Electronics Laboratory, University of California, Los Angeles, CA 90095, USA.

³ Institute of Microelectronics, A*STAR, Singapore 117865, Singapore.

⁴ Department of Physics, Columbia University, New York, NY 10027, USA.

⁺ These authors contribute equally.

^{*} Author e-mail: swhuang@seas.ucla.edu ; yangjh@seas.ucla.edu ; cheewei.wong@ucla.edu

I. Spontaneous Turing pattern formation through modelled Lugiato-Lefever dynamics

In our model we numerically studied the Turing roll formation using the Lugiato-Lefever equation (LLE), $T_R \frac{\partial}{\partial t} A(t, \tau) = \sqrt{\alpha_c} A_{in} - \left[\frac{\alpha_c + \alpha_p}{2} + j\delta + j\bar{D}L + j \frac{n_2 \omega L}{c} I(t, \tau) \right] A(t, \tau)$, for its computational efficiency [S1]. Here α_p is the propagation loss, α_c is the coupling loss, δ is the detuning, and $\bar{D} = \sum_{n \geq 2} \frac{\beta_n}{n!} \left(-j \frac{\partial}{\partial \tau} \right)^n$ is the dispersion operator. The LLE was solved for 2,001 modes around the cw pump. The simulation started from vacuum noise and was run for 10^6 roundtrips until the solutions reached the steady state.

In the anomalous dispersion regime, a spontaneous growth of symmetric Turing roll was observed. As the wavelength was tuned closer to resonance, sub-comb started to emerge and destabilize the Turing pattern. The evolution dynamics with on-chip pump power of 100 mW (along the white dashed line of Figure 1a) is shown in Figure S1. On the other hand, growth of Turing roll is prohibited in the normal dispersion regime unless local dispersion disruption by mode hybridization is introduced (Figure 1c). To account for the local dispersion disruption, we artificially changed the resonance frequency of the -14^{th} cavity mode such that $2\omega_0 - \omega_{14} - \omega_{-14}$ is phase matched. Then a spontaneous growth of Turing pattern was observed, but clearly the spectral symmetry was broken. Furthermore, sub-comb growth and transition into chaos were forbidden. The dispersion employed in the simulation is validated by both numerical modeling

and experimental measurement for microrings with different radii, as plotted in Figure S2, featuring not only a high GVD but also a large third-order dispersion. The ring radius is designed to be large enough ($>160 \mu\text{m}$) such that the bending-induced dispersion is negligible. The measured GVDs at 1603 nm (circles with error bars) show good agreements with the numerical modeling by finite-element analysis.

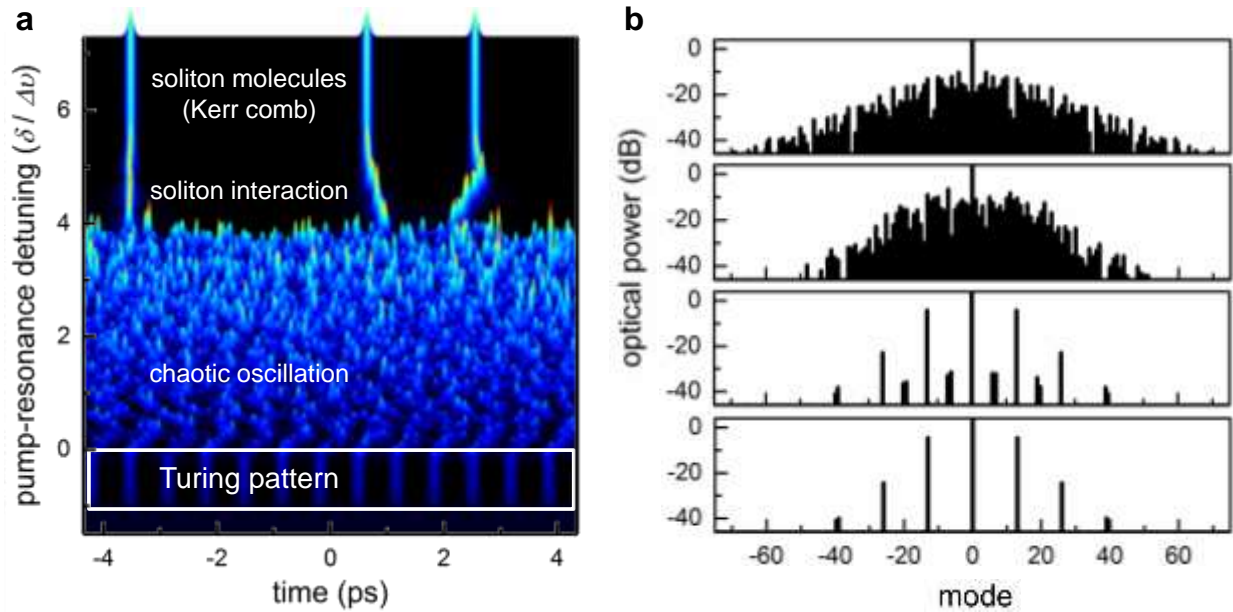


Figure S1 | Evolution dynamics in (a) temporal domain and (b) spectral domain, along the white dashed line in Figure 1a. Spontaneous Turing pattern is formed, then quickly collapsed into spatio-temporal chaos, and eventually transformed into soliton molecules with a proper scan protocol of pump detuning.

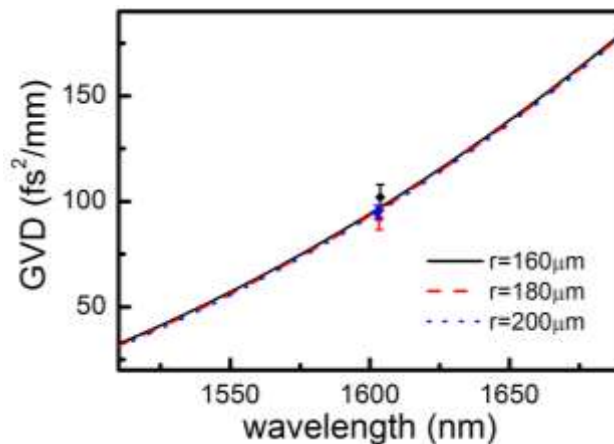


Figure S2 | Group velocity dispersion (GVD) of our ring resonators, featuring large normal GVDs of $+100 \text{ fs}^2/\text{mm}$. The ring radius is designed to be large enough (more than $160 \mu\text{m}$) such that the bending-induced dispersion is negligible. Measured GVDs at 1603 nm (circles with error

bars) show good agreements with the numerical modeling. Inset: scanning electron micrograph of the nonlinear ring resonator. Scale bar: 50 μm .

II. Dynamic tuning of mode hybridization by device temperature control

A series of simulated cavity resonances by 3D finite-element analysis [S6] is shown in Figure S3a. *Mode 0* is where the resonance frequencies of the two mode families (ω_{11} and ω_{12}) cross each other. The exact crossing point is determined by the distinct free spectral ranges (FSRs) of the two transverse modes (TM_{11} and TM_{21}), and it can be tuned by design of the waveguide geometry. Here without considering modal interaction effect, as Figure S3b shows, the frequency difference can be simply expressed as $\Delta_{\text{eig}}/2\pi = (\omega_{11} - \omega_{12})/2\pi$ and it has a linear relationship with the mode number.

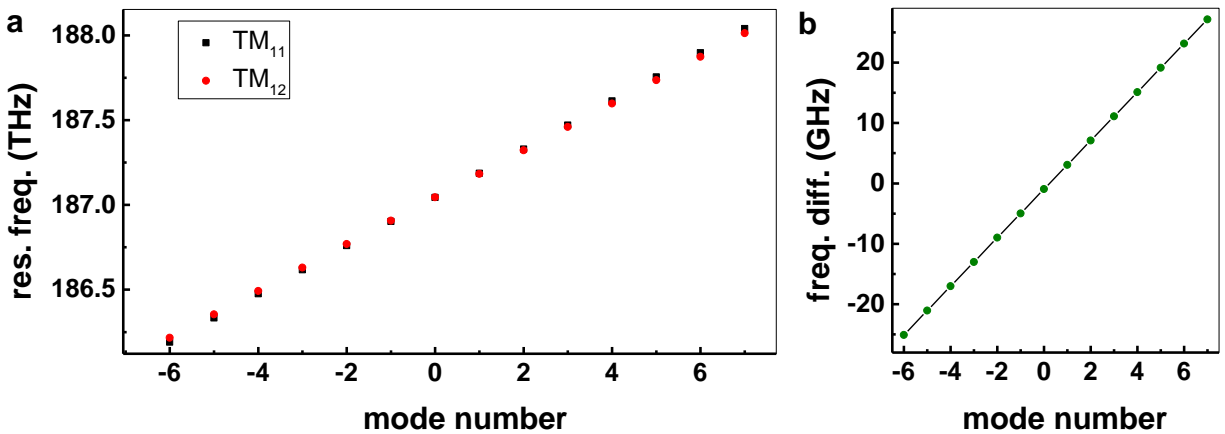


Figure S3 | Numerically modeled cavity resonances and mode crossing. (a) Resonance frequencies of TM_{11} ($\omega_{11}/2\pi$, black square) and TM_{12} ($\omega_{12}/2\pi$, red dot) at the temperature of 60 $^{\circ}\text{C}$. (b) Frequency difference between TM_{11} and TM_{12} mode, *i.e.*, $\Delta_{\text{eig}}/2\pi$, showing a linear relationship with mode number. The crossing point between the two mode families is a function of FSR difference and can be tuned by design of the waveguide geometry.

In real devices, however, the two modes can couple with each other when their resonance frequencies are close, owing to imperfections in material growth, waveguide cross-section, and bending geometry. Figure S4a plots the experimentally measured resonance frequencies for the two modes at the temperature of 60 $^{\circ}\text{C}$. Figure S4b shows the frequency differences calculated from the measurements at two different temperatures of 60 $^{\circ}\text{C}$ and 70 $^{\circ}\text{C}$ respectively; at *mode 0*, the cavity mode experiences a frequency shift Δ_m , leading to an offset from the otherwise linear relationship (blue lines) between the frequency difference and the mode number. Of note, Figure

S4c shows that Δ_m is inversely proportional to Δ_{eig} and their exact values are temperature dependent. Both relationships are consistent with the coupled mode theory elaborated later in details.

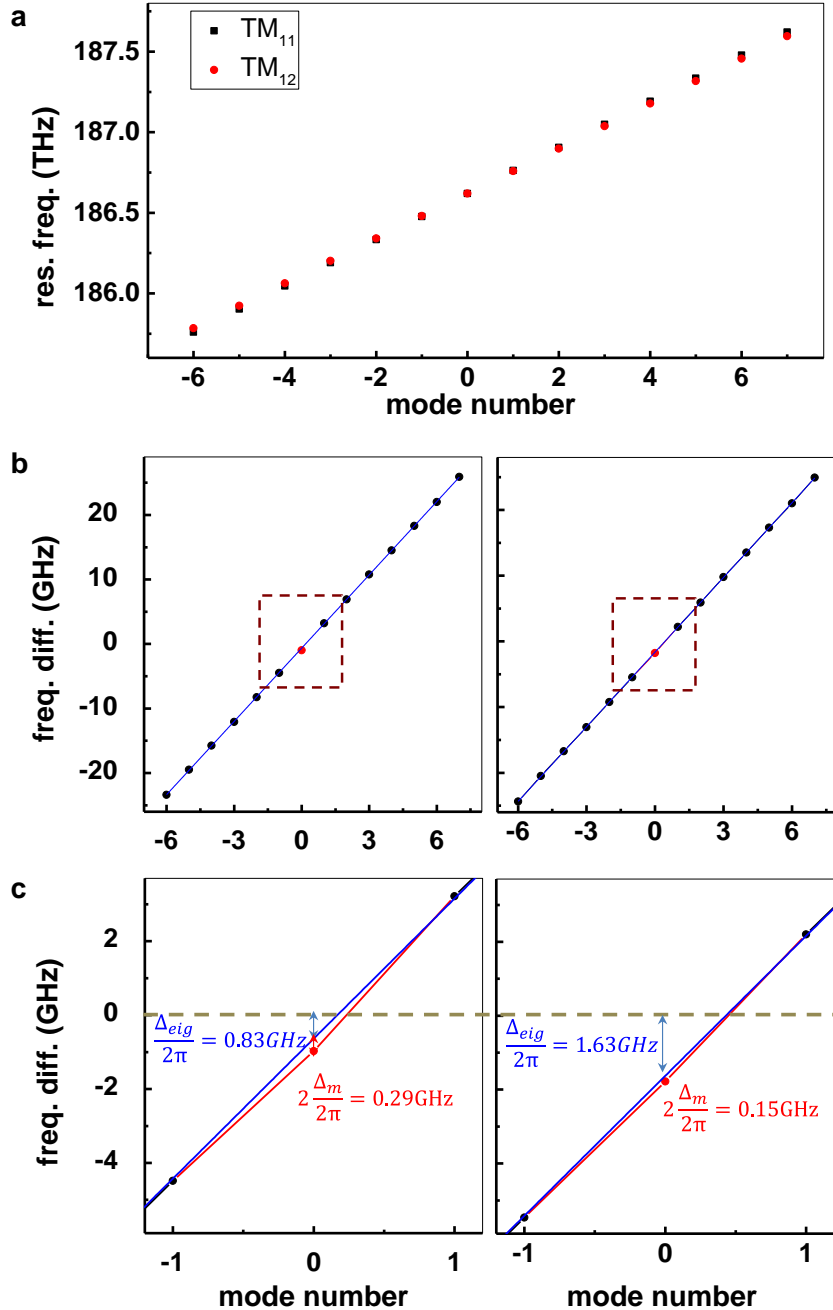


Figure S4 | (a) Experimentally measured resonance frequencies of TM₁₁ (black square) and TM₁₂ (red dot) at the temperature of 60 °C. (b) Frequency difference between TM₁₁ and TM₁₂ at 60 °C (left) and 70 °C (right). (c) Zoom-in frequency difference around *mode 0*. The linearly fitted value at *mode 0* is the frequency difference between the two

eigenmodes $\Delta_{\text{eig}}/2\pi$, 0.83 GHz at 60 °C and 1.63 GHz at 70 °C, without considering the modal interaction effect; the additional offset from the measurement (red dot) shows the modal frequency shift induced by mode hybridization $\Delta_{\text{m}}/2\pi$, 0.29 GHz at 60 °C and 0.15 GHz at 70 °C.

From the coupled mode theory, Δ_{eig} and Δ_{m} have a fixed relationship in a given device $\Delta_{\text{m}} = -\frac{\kappa^2}{\Delta_{\text{eig}}}$ [S2, S5], where κ is the mode interaction constant. Of note, while it is very challenging to control the mode interaction constant, adjusting Δ_{eig} through either waveguide design or dynamic temperature tuning is an effective way to engineer the overall effect of mode hybridization. When the magnitude of temperature tuning is sufficiently high, it can even shift the mode hybridization position, a phenomenon that is later utilized for discrete tunability of THz frequency. A summary of all measured Δ_{eig} at the temperature ranging from 30 °C to 90 °C are shown in Figure S5 (red dots). An analytic fit is performed based on the relation $R_0(1 + \alpha\Delta T)n_0 \left(1 + \frac{1}{n_0} \frac{dn}{dT} \Delta T\right) \omega = mc$ [S6], where R_0 is the original ring radius, n_0 the original index, ΔT the temperature change, m the mode number, $\frac{dn}{dT}$ the thermal optic coefficient, and α the thermal expansion coefficient [S7]. A better fit to the measurement data points (blue line) can be obtained by adjusting $\frac{dn}{dT}$ from $2.45 \times 10^{-5} / \text{°C}$ as reported in the literature [S7] to $1.76 \times 10^{-5} / \text{°C}$. To further validate our results, we calculate the mode interaction constant κ as a function of temperature using the measured Δ_{eig} and Δ_{m} . As expected, κ is practically temperature invariant from 50 °C to 70 °C, with a mean value of 2.1 GHz and a standard deviation of 2 % (Figure S6).

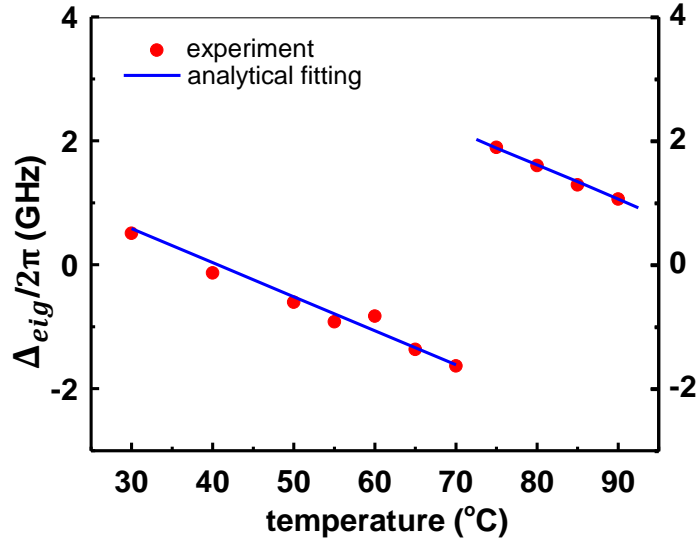


Figure S5 | Tuning of Δ_{eig} through chip temperature control, which in turn change the mode hybridization effect. Δ_{eig} shows a linear relationship with temperature. When the chip temperature is increased to more than 75 °C, the mode hybridization effect shifts to the adjacent mode.

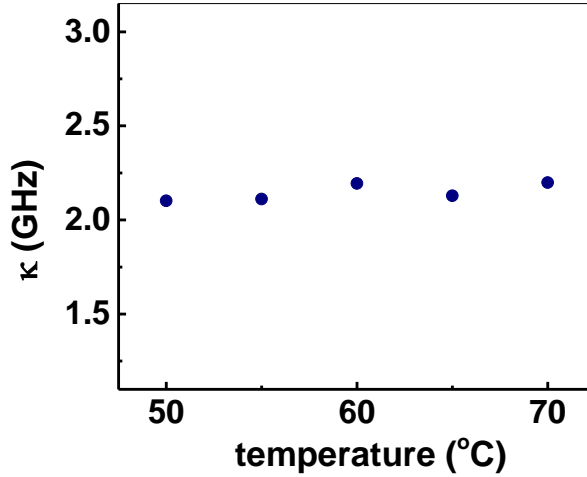


Figure S6 | Mode interaction constant κ derived from experimental measurements using the equation $\Delta_m = -\frac{\kappa^2}{\Delta_{eig}}$. Across all temperatures, the κ is consistently 2.1 GHz with 2% standard deviation.

To complete our discussion, we next quantitatively examine the mode hybridization mediated phase matching as outlined in the main text. The wavenumber with mode hybridization effect (k_1) and without mode hybridization effect (k_{10}) can be written as:

$$k_1 = k_0 + \beta'(\Delta + \Delta_m) + \frac{\beta_2}{2}(\Delta + \Delta_m)^2$$

$$k_{10} = k_0 + \beta'\Delta + \frac{\beta_2}{2}\Delta^2$$

hence the phase mismatch induced by mode hybridization can be expressed as $\varepsilon = k_1 - k_{10} \approx \beta'\Delta_m + \beta_2\Delta \cdot \Delta_m$. Consequently, a modal frequency shift of $\Delta_m \approx \frac{\beta_2\Delta^2 + \gamma P_{\text{int}}}{\beta'}$ is required to satisfy the phase matching condition, $\Delta k(2\omega_0 - \omega_1 - \omega_{-1}) = \beta_2\Delta^2 + \gamma P_{\text{int}} - \varepsilon = 0$. Plugging in the measured $\Delta_m/2\pi$, $\Delta/2\pi$, β_2 , β' , and γ , we find the required intra-cavity power of 15 W is in a good agreement with the experiment.

III. Definition of pump-to-comb power conversion efficiency

As shown in Figure S7, here the pump-to-comb power conversion efficiency is defined as:

$$\eta = \frac{\int_0^T (I_{\text{out}} - I_{\text{bkg}}) dt}{T}$$

In the calculation, we only consider the optical power of the Turing pattern carried by the output bus waveguide. This definition of power conversion efficiency, rather than slope efficiency or internal efficiency, is adopted in this manuscript because it provides a more transparent measure to calculate the total available power for real-world applications.

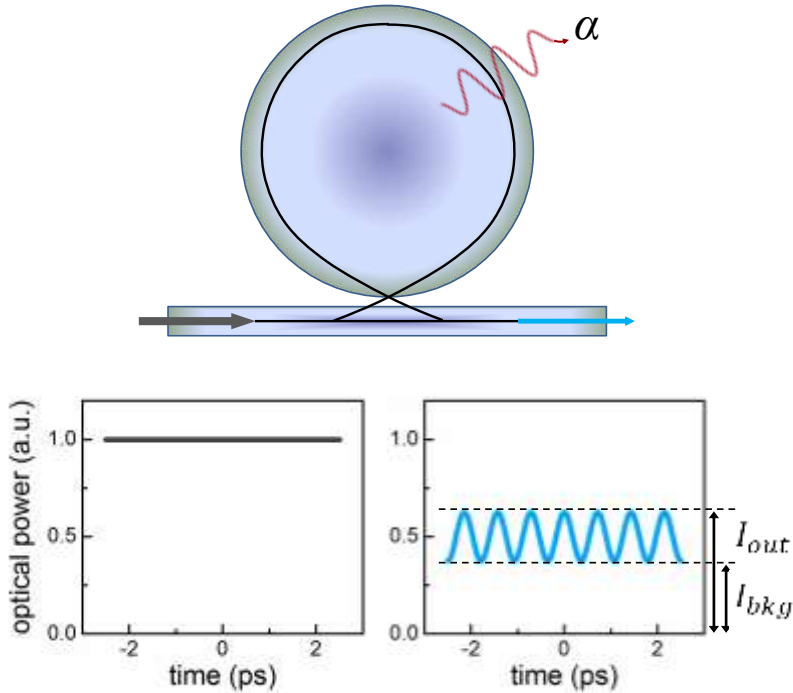


Figure S7 | Illustration of external pump-to-comb conversion efficiency.

IV. Turing rolls for coherent high-power tunable THz generation

Figure S8 shows the intensity autocorrelation (IAC) profile of the Turing roll at the stage III. Due to the efficient energy conversion from the pump to the first sideband pair, the Turing roll features a quasi-sinusoidal intensity profile with a negligible background of less than 1% of the peak intensity. Nearly background-free operation is important for efficient on-chip THz generation as it reduces the risk of thermal breakdown at high optical pump powers.

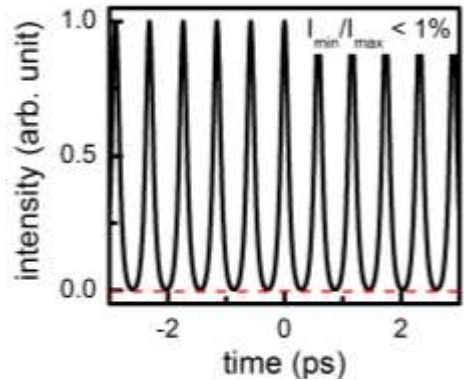


Figure S8 | Measured intensity profile of the sub-picosecond Turing roll, showing a quasi-sinusoidal oscillation with a more than 100 contrast.

V. Temporal dynamics of the Turing pattern formation

To probe the robustness of the Turing pattern formation to the perturbations in initial conditions and pump wavelength tuning speeds, we recorded IAC traces of the Turing rolls generated under three different tuning speeds on two different days. The results are summarized in Figure S9. Unlike the microresonator soliton generation where the initial condition and the tuning speed play key roles in determination of the soliton states, here the Turing roll always evolves in the identical route and is robust against perturbations in initial conditions and pump wavelength tuning speeds.

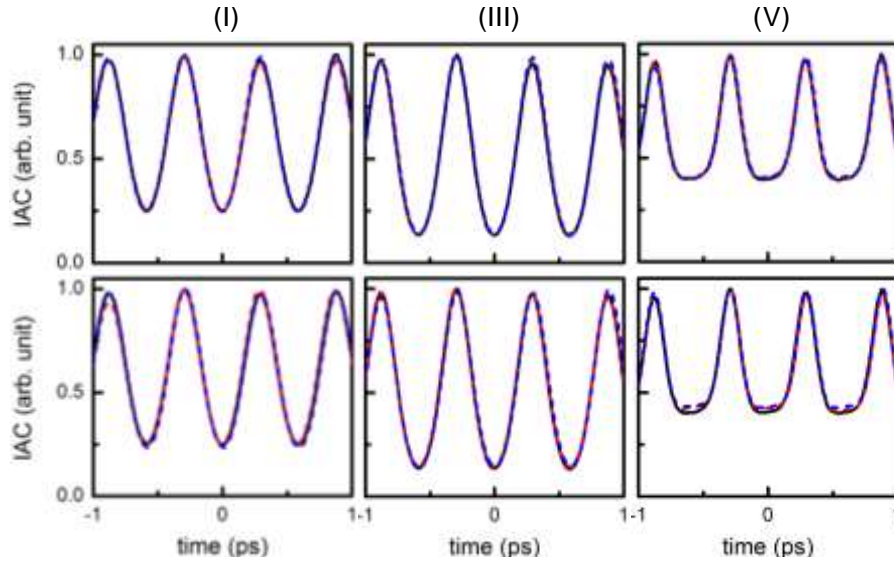


Figure S9 | At three different scanning speeds (black curve: 1 nm/s; red dashed curve: 0.3 nm/s; blue dashed curve: 0.1 nm/s) and two independent starts (top and bottom), the Turing roll shows the identical generation route.

Figure S10 illustrates how applying an additional dispersion (30 cm SMF28) leads to different temporal structure changes of the Turing pattern at two example detunings. The effect can be understood as the consequence of the pump phase slip around the resonance. As shown in Figure S11a, the output pump will experience a π phase shift as it traverses through the resonance. Such phase slip is due to the interference between the intracavity and the input pump and thus the other sidebands of the Turing roll will not experience such a phase shift. This additional pump phase slip results in the observed change of temporal structure. The distinct responses to dispersion illustrated in Figure S10 are well captured by considering the pump phase offset (Figure S11). Of note, most of the phase slip happens very close to cavity resonance and thus the observation of its effect is attributed to the unique design of our microresonator, where the effect of mode hybridization mediated phase matching of spontaneous Turing pattern formation prevents the Turing pattern destabilization even when the pump is deep into the resonance.

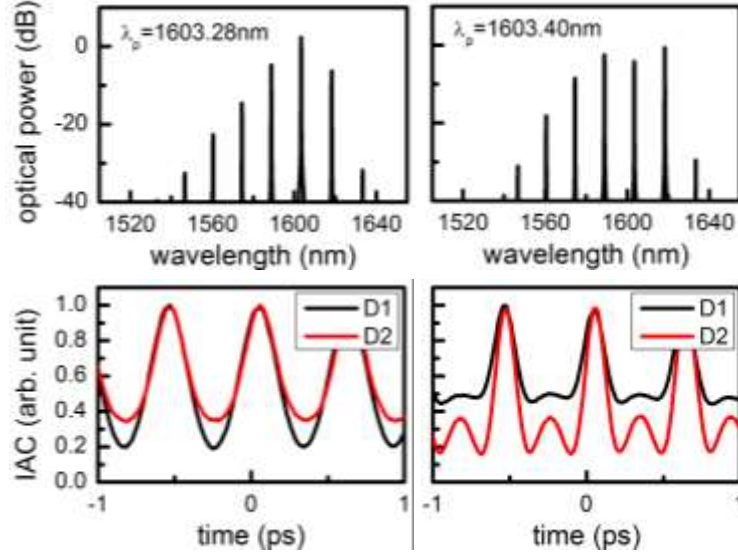


Figure S10 | IAC traces of the Turing rolls at two different pump detunings ($\lambda_p = 1603.28$ nm and $\lambda_p = 1603.40$ nm) with two external dispersion compensation. Here D1 and D2 use 60 cm and 90 cm SMF-28 fibers as the external dispersion elements, respectively.

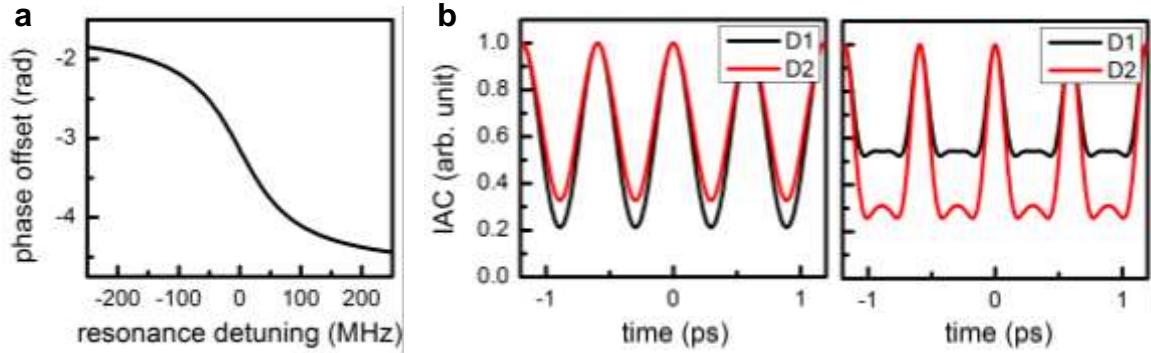


Figure S11 | (a) Phase offset between the intracavity and output pump light, showing a π phase slip around the resonance. (b) IAC traces calculated by adding $\pi/2$ to the pump wavelength for $\lambda_p = 1603.40$ nm, showing a good agreement with the measurements shown in Figure S10.

VI. Microresonator characterizations and Turing pattern measurements

Figure S12 shows the schematic diagram of the dispersion measurement setup [S5]. The microresonator transmission was recorded when the laser was swept from 1550 nm to 1630 nm at a tuning speed of 40 nm/s. The sampling clock of the data acquisition is derived from the photodetector monitoring the laser transmission through a fiber Mach-Zehnder interferometer with 40 m unbalanced path lengths, which translates to a 5 MHz optical frequency sampling resolution. Transmission of the hydrogen cyanide gas cell was simultaneously measured and the absorption features were used for absolute wavelength calibrations. Each resonance was fitted

with a Lorentzian lineshape to determine the resonance frequency and the quality factor. The microresonator dispersion was then calculated by analyzing the wavelength dependence of the free spectral range.

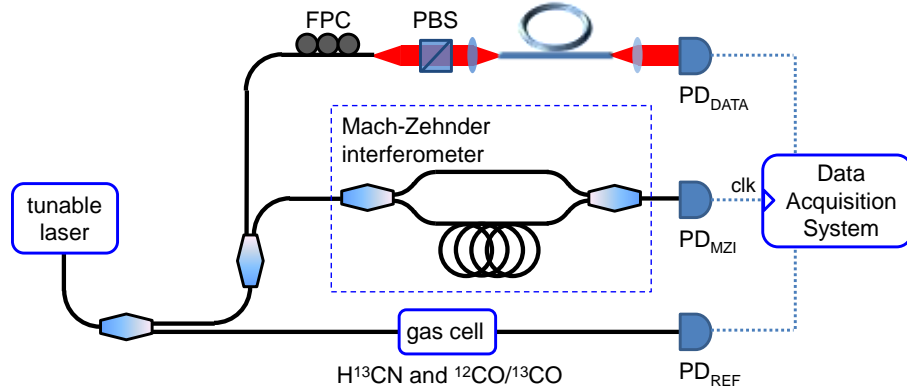


Figure S12 | Microresonator dispersion measurement setup.

To probe the equidistance of the Turing roll sidebands, a uniformity measurement setup is employed as shown in Figure S13. The generated Turing roll was split and sent to 3 beat detection units (BDUs) individually optimized for the wavelength of the pump (1603 nm), the 1st sideband (1589 nm), and the 2nd sideband (1575 nm). Heterodyne beat notes were generated between the Turing roll (green arrows) and a reference fiber laser frequency comb (red arrows). The gratings in the BDUs critically suppress the unwanted reference fiber laser frequency comb teeth such that clean heterodyne beat notes with more than 40 dB signal to noise ratio (measured with a 100 kHz resolution bandwidth), sufficient for reliable measurements, can be routinely obtained. The beat notes from the sidebands (δ_1 and δ_2) were mixed with the beat note from the pump (δ_0) to cancel the residual pump wavelength instability before being measured by a high-resolution frequency counter (10 mHz frequency error at 1 second). The frequency counter was operated in the ratio counting mode, to circumvent the synchronization challenge of simultaneous beat note measurements and achieve a more accurate measurement.

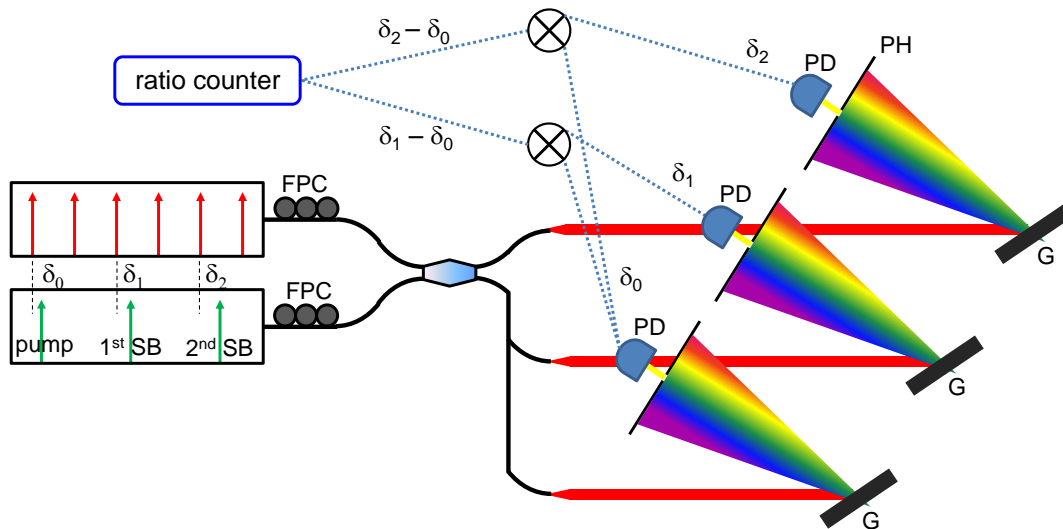


Figure S13 | Turing pattern sideband frequency uniformity measurement setup.

Figure S14 shows the schematic diagram of the self-heterodyne linewidth measurement setup [S8]. The input was split into two parts with 70% of it being sent through an acousto-optic modulator which shifts the optical frequencies by 200 MHz. The other portion was sent through a 5 km single mode optical fiber, providing a time delay of 24.5 μ s. Both lights were then recombined, and the resulting beat note was recorded and analyzed with a high-speed photodetector and an electrical spectrum analyzer. The RF spectrum becomes a self-convolution of the laser spectrum, from which the linewidth can be retrieved, as long as the coherence length is shorter than the introduced delay. Thus our self-heterodyne measurement setup can measure a minimum linewidth at 13 kHz, about 40 times smaller than the measured laser linewidth.

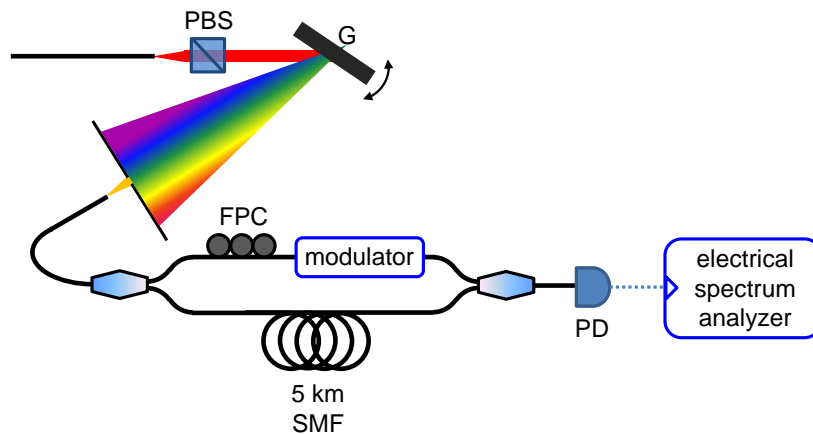


Figure S14 | Self-heterodyne measurement setup.

Figure S15 shows the schematic diagram of the linewidth and drift of the THz carrier measurement setup. The pump and one of the sideband are beat with the adjacent fiber laser frequency comb lines, and two beat signals are electrically mixed to get the beat note of the frequency difference.

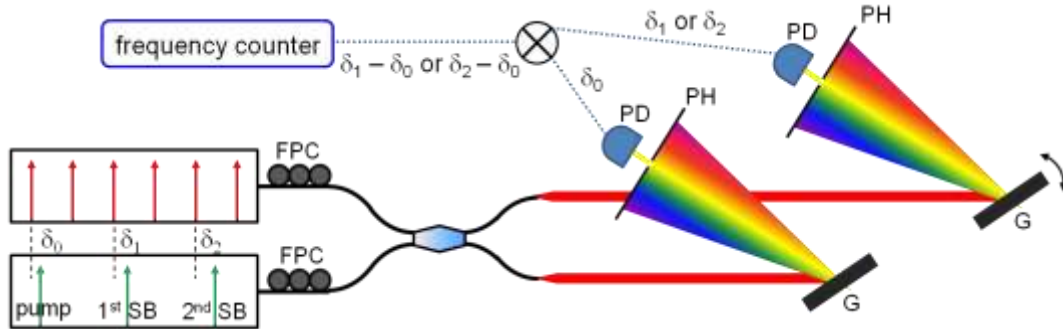


Figure S15 | Turing pattern frequency stability characterization setup.

Figure S16 shows the schematic diagram for THz frequency stabilization setup. The first Turing sideband is filtered out and sent to a photodetector to monitor the power fluctuation. A computer program is used as the loop filter that takes in the Turing sideband power fluctuation as the error signal and outputs the control signal to modulate the pump power. The computer-aided slow feedback loop has a bandwidth of 1 Hz.

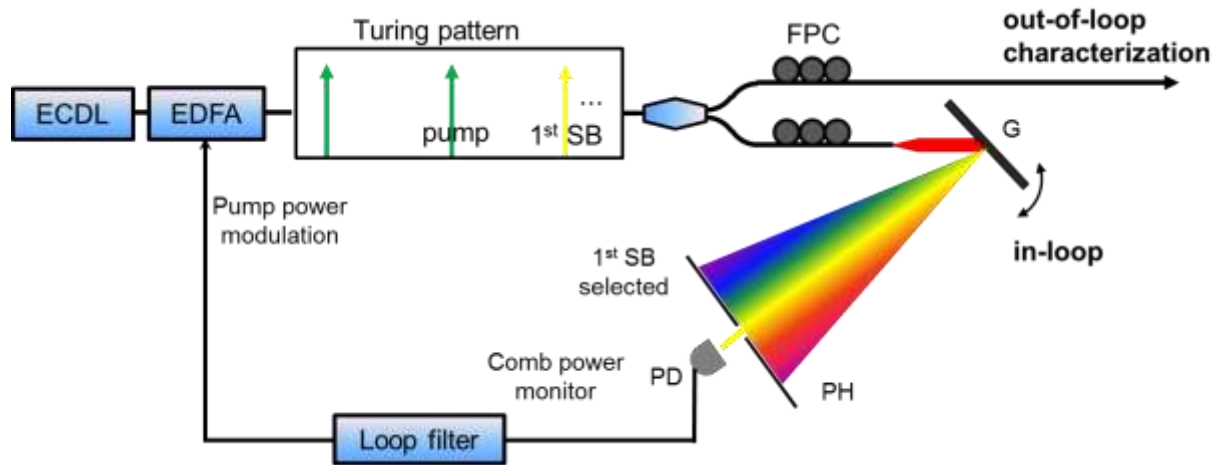


Figure S16 | Turing pattern frequency stabilization setup.

Figure S17 shows the schematic diagram of the THz radiation generation setup. A C/L WDM filter, followed by an erbium doped fiber amplifier (EDFA), was used to selectively amplify the Turing roll sidebands in the 1530 to 1565 nm C-band range. A 500 kHz intensity modulator was utilized to reduce the duty cycle of the Turing roll to 1%, thereby increasing the

thermal breakdown onset threshold. Efficient photomixing [S3] is achieved based on a logarithmic spiral plasmonic antenna design [S4] for efficient THz radiation generation. To achieve the highest photomixing efficiency, both the focus spot size and the position of the optical pump were adjusted to maximize the induced photocurrent level. The generated THz radiation was then measured with a liquid helium-cooled silicon bolometer. Lock-in detection technique was implemented to reduce the noise level and obtain a more reliable reading of the THz radiation power.

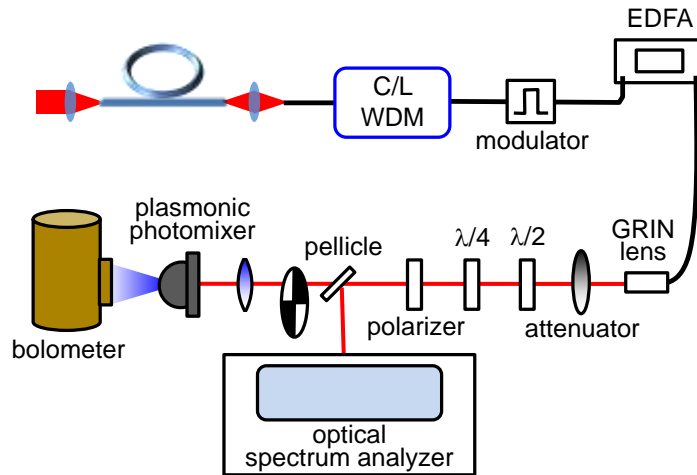


Figure S17 | THz radiation generation setup.

Supplemental References:

- [S1] S. Coen, H. G. Randle, T. Sylvestre, and M. Erkintalo, "Modeling of octave-spanning Kerr frequency combs using a generalized mean-field Lugiato–Lefever model," *Opt. Lett.* **38**, 37 (2013).
- [S2] A. A. Savchenkov, A. B. Matsko, W. Liang, V. S. Ilchenko, D. Seidel, and L. Maleki, "Kerr frequency comb generation in overmoded resonators," *Opt. Express* **20**, 27290 (2012).
- [S3] H. Tanoto, J. H. Teng, Q. Y. Wu, M. Sun, Z. N. Chen, S. A. Maier, B. Wang, C. C. Chum, G. Y. Si, A. J. Danner, and S. J. Chua, "Nano-antenna in a photoconductive photomixer for highly efficient continuous wave terahertz emission," *Sci. Rep.* **3**, 2824 (2013).
- [S4] C. W. Berry, M. R. Hashemi, S. Preu, H. Lu, A. C. Gossard, and M. Jarrahi, "High power terahertz generation using 1550 nm plasmonic photomixers," *Appl. Phys. Lett.* **105**, 011121 (2014).
- [S5] S.-W. Huang, H. Zhou, J. Yang, J. F. McMillan, A. Matsko, M. Yu, D.-L. Kwong, L. Maleki, and C. W. Wong, "Mode-locked ultrashort pulse generation from on-chip normal dispersion microresonators," *Phys. Rev. Lett.* **114**, 053901 (2015).

- [S6] L. Zhang, Y. Yue, R. G. Beausoleil, and A. E. Willner, "Analysis and engineering of chromatic dispersion in silicon waveguide bends and ring resonators," *Opt. Express* **19**, 8102 (2011).
- [S7] A. Arbabi and L. L. Goddard, "Measurements of the refractive indices and thermo-optic coefficients of Si_3N_4 and SiO_x using microring resonances," *Opt. Lett.* **38**, 3878 (2013).
- [S8] T. Okoshi, K. Kikuchi, and A. Nakayama, "Novel method for high resolution measurement of laser output spectrum," *Electron. Lett.* **16**, 630 (1980).